Supporting Information for

Spatial and spectral mode mapping of a dielectric nanodot by broad-band interferometric homodyne scanning near-field spectroscopy

Jinxin Zhan, Wei Wang, Jens Brauer, Lukas Schmidt-Mende,
Christoph Lienau, and Petra Groß

1 Sample preparation

A 40-nm thick compact TiO_2 film was prepared by sputtering TiO_2 on a fluorine doped tin oxide (FTO) glass substrate. Subsequently, a 180-nm thick Sb_2S_3 precursor film was deposited by spin-coating an Sb_2S_3-complex solution diluted with ethanol (ratio 2 to 1)[47] at a speed of 8000 rpm for 30 s. After spin-coating, the substrate was baked at 140 °C for 1 min, which resulted in the formation of an orange-red amorphous Sb_2S_3 thin film. The substrates were transferred into a glove box to anneal at 300 °C for 30 min, forming a 140-nm thick, compact, crystalline Sb_2S_3 film. On top of this dense Sb_2S_3 film, a second, 100-nm thick Sb_2S_3 film was deposited as a precursor for the nanostructure fabrication, by spin-coating an Sb_2S_3-complex solution diluted with ethanol. We directly transferred the obtained substrate into the electron beam lithography (EBL) system (Elphy nanolithography based on Zeiss Neon 40EsB 30 keV scanning electron microscopy) for electron beam patterning (EBP) with a typical dose of 36.000 μC/cm^2 at 20 keV. After the EBL process, the substrates were annealed at 300 °C for 30 min in a glove box. At last, the patterned Sb_2S_3 nanoparticle array was developed with acetone rinse.

2 Details on the near-field probe

The single-crystalline gold nanotips are produced from polycrystalline, 99.99%-gold wire with a diameter of 125 μm. The gold wire is annealed and electrochemically etched as described in Ref. 48. We select a taper with a smooth surface, an opening angle of 20°-30°, and with a small apex radius of curvature of about 10 nm to glue onto a tuning fork. The taper is then aligned with its axis along the *z*-axis, i. e., the sample surface normal, and the tuning fork is driven with an AC voltage at its resonance frequency $f \approx 26\,\mathrm{kHz}$ and such that the tip moves back and forth along the *z*-axis with an amplitude of about 12 nm. The tip-sample distance is controlled by adjusting the sample *z*-position using the tuning fork oscillation amplitude as the feedback signal in a tapping-mode atomic force microscope. With the tip in close vicinity to the sample surface, i. e., with a minimal tip-sample distance of ~4 nm, the focus position is aligned to maximize the back-scattered signal. The light is incident with the *k*-vector in the *x*-*z*-plane, at an angle of 70° to the surface normal. Here, we set the light polarization to *s*, i. e., the electric field vector is along the *y*-axis, such that it lies within the sample plane and is perpendicular to the tip axis. During a measurement, the positions of the tip and the laser focus are fixed, and the sample can be moved in three dimensions.

3 Demodulated near-field spectra

In order to obtain spectrally resolved near-field measurements, the signal scattered out of the focus area on the sample by the near-field probe is superimposed with the reference field. This is realized by employing a Michelson interferometer with a broad-bandwidth 20:80 beam splitter (see sketch of the setup in Fig. 1 of the main manuscript). 20% of the incident light intensity enters the sample path, which contains a reflective microscope objective (MO, Beck Optronics Solutions, model 5003-000), and the sample and near-field probe. Light scattered back from the tip-sample direction is collected by the same MO. The larger part, 80% of the incident light enters the reference arm, which contains a variable grey filter for power adjustment and a mirror for direct back reflection. Light from the two arms is superimposed at the beam splitter for spectral measurements. The length of either arm is about 150 mm, where the reference arm is shorter than the sample arm by about 100 µm. This results in spectral interference fringes with a fringe spacing of about 3 nm, which is a convenient spacing for the following evaluation. The interferometer including the near-field probe and sample is housed inside a foam-covered box for acoustic noise suppression. We find that the reference arm mirror typically jitters within ± 50 µm during a measurement of 280 ms duration, taken at one position of a SNOM scan. The change of the optical path length difference $(\pm 100\ \mu\mathrm{m})$ is sufficiently small that an active length stabilization can be avoided.

The light collected from the Michelson interferometer is dispersed with a monochromator (Princeton Instruments, IsoPlane-160), and the spectra are recorded with a fast line camera (e2V Aviiva EM4 with 512 pixels). The line camera has a maximum readout rate of 210 kHz. The line acquisition is not synchronized to the tip, which is modulated at its resonance frequency of around 26 kHz. Instead, the camera data is stored at the maximum available line rate and the signal modulations occurring at each pixel at multiples of the tip modulation frequency are extracted in a post-processing Fourier analysis. The working principle of such pixel-wise demodulation and spectrally resolved near-field measurements were introduced first in Ref. 44, but in that case the reference field was introduced by an in-line interferometer with small, fixed distance (~0.5 µm) from the sample plane. Here, we make use of this procedure for obtaining near-field spectra from the data recorded by the fast line camera with a reference arm length detuning of ~100 µm.

4 Simulated near-field spectra

In the main manuscript Fig. 5 we have presented calculated near field spectra, in order to show that the measured $S_{4f}(\lambda)$ spectra agree well with our expectations. Here we give details of the underlying calculations.

For the present experiments, with an incident field that is polarized parallel to the sample surface, we only consider the in-plane polarizability of the gold tip. We model the tip as a point dipole located at the center of a gold sphere with radius $R = 10\ \mathrm{nm}$ and with an isotropic

polarizability of a gold sphere: $\alpha_{tip} = 4\pi\varepsilon_0 \cdot R^3 \left(\varepsilon_{Au} - \varepsilon_{air}\right)\left(\varepsilon_{Au} + 2\varepsilon_{air}\right)^{-1}$. Here, ε_{Au} and ε_{air} are the dielectric functions of gold from Ref. 49 and of air, respectively. Usually, the assumption of such an isotropic tip response is not well justified. The sharp metal tapers show an intense and spectrally broadband component of their polarizability tensor that is oriented along the taper axis (z-axis),[35,41,50,51] that results in a local field enhancement at the apex of 7-10 in the near-infrared range.[52] For the present experiments, the z-component of the polarizability tensor is of minor importance since the incident light is polarized along the *y*-direction $\vec{E}_{inc} = E_{inc}\hat{y}$, and since also the optical modes of the nanodot are mainly polarized within the sample plane, with little *z*-component of their fields. Following Knoll and Keilmann,[40] this in-plane tip dipole causes a *y*-polarized material polarization in the sample, which re-emits a field acting back on the tip dipole. The tip response can then be described by an effective polarizability

$$\alpha_{eff}\left(d\right) = \frac{\alpha_{tip}}{1 - \frac{\alpha_{tip}\beta}{32\pi\varepsilon_0\left(R+d\right)^3}} \tag{1}$$

Here, $\beta = \left(\varepsilon_{Sb_2S_3} - 1\right)\left(\varepsilon_{Sb_2S_3} + 1\right)^{-1}$ is the material response with the dielectric function of Sb_2S_3, and *d* is the tip-sample distance. The total response of the coupled tip-sample system is then $\alpha_{eff}\left(d\right)\left(1-\beta\right)$.

The effective tip polarizability is plotted as a function of wavelength for the same tip-sample distances *d* as were measured in the experiment in Fig. 5(c) in the main manuscript. The effective polarizability increases as the tip-sample distance decreases. There is an increase towards short wavelengths, which is caused by the far detuned tip resonance. This spectral shape is preserved during the approach.

The near field radiated by the tip at position $\vec{r}\,'$ and detected at position $\vec{r}$ is calculated by applying the dyadic Green's function $\ddot{G}$:

$$\vec{E}_{NF}\left(\vec{r},d\right) = \ddot{G}\left(\vec{r},\vec{r}\,'\right)\ddot{\alpha}_{eff}\left(d\right)\vec{E}_{inc} \tag{2}$$

Since the tip is excited by a linearly polarized incident electric field and we assume an isotropic tip polarizability and isotropic material polarizability, it is sufficient to only consider one polarization component, in our case the *y*-component. We calculate the dipole field component that is radiated towards the detector and mix it with the reference field to yield the measured near-field spectrum $S_{NF}\left(\lambda,d\right)$ for the different distances *d*:

$$S_{NF}\left(\lambda,d\right) \propto k^2\ \mathrm{Re}\left\{\left(\ddot{\alpha}_{eff}\left(\lambda,d\right)\right)_{yy} E_R\left(\lambda\right)E_{inc}\left(\lambda\right)\right\} \tag{3}$$

Finally, one has to take into account the demodulation process that reduces the signal to its AC components. The result calculated by Eqs. 1-3 are the near-field spectra shown in Fig. 5(d).

5 Projected local optical density of states

In order to explain the measured spatial function of the waveguide modes, shown in Figs. 3 and 7 of the main manuscript, we have calculated the projected local optical density of states (LDOS). In the spectral region covered by the laser in this work, the nanodot material shows negligible absorption and very weak dispersion. In the main manuscript, we show that under these conditions the nanodot supports eigenmodes, which are very similar to the well-known modes of an optical fiber. Here we describe the calculations used to derive the projected LDOS, which we compare to the measured near-field maps.

In our near-field measurements, a sharply etched gold nanotaper is scanned across the outer surface of the nanodot. The nanotaper is placed in the focus of a laser, which creates a dipole of fixed orientation, along a direction $\hat{u}$. In principle, if such a dipole is scanned across a surface, it probes the LDOS projected on the direction $\hat{u}$:[26,13]

$$\rho_{\hat{u}}(\vec{r},\omega) = \frac{2\omega}{\pi c^2}\,\mathrm{Im}\left[\hat{u}\cdot\ddot{G}(\vec{r},\vec{r},\omega)\cdot\hat{u}\right], \tag{4}$$

where $\ddot{G}(\vec{r},\vec{r},\omega)$ is the dyadic Green's function. Here, we scan the tip across the surface of a nanostructure with a set of discrete eigenmodes, with eigenvectors $\vec{e}_m(\vec{r})$ and eigenfrequencies ω_m, which are solutions of the vector Helmholtz equation. The eigenvectors are orthonormal:

$$\int_V \varepsilon(\vec{r})\cdot\vec{e}_m(\vec{r})\cdot\vec{e}_n^{\,*}(\vec{r})\,d^3r = \delta_{mn} \tag{5}$$

with $\varepsilon(\vec{r})$ the dielectric function of the material. The local density of states (LDOS) is introduced following Carminati *et al*.[26] as a summation over the eigenmodes, weighed by their amplitudes at position $\vec{r}$:

$$\rho(\vec{r},\omega) = \sum_m \left|\vec{e}_m(\vec{r})\right|^2 \delta_g(\omega-\omega_m), \tag{6}$$

where δ_g is a generalized Dirac delta function. The Green's function in Eq. 4 then becomes:

$$\ddot{G}(\vec{r},\vec{r},\omega) \approx \sum_m c^2 \frac{\vec{e}_m^{\,*}(\vec{r})\otimes\vec{e}_m(\vec{r})}{\omega_m^2-\omega^2-2i\omega\gamma_m} \tag{7}$$

This is the Green's function for weakly dissipative systems, where we have included as small damping rate γ_m for mode *m*. In order to retrieve the eigenmodes, we first performed FDTD simulations of a Sb_2S_3 nanodot.[53] We modelled the structure as a cylinder with 200 nm radius and 75 nm height, capped with a semi-ellipse on top. The total height was 150 nm, and the structure was placed on a 100-nm thick film. For both the film and the structure we applied the experimentally measured refractive index function of Sb_2S_3, which varies from 3.2 at 700 nm to 2.9 at 900 nm. The solution for the modes identified by the FDTD solver in the structure, in the *xy*-plane parallel to the surface of the film, are shown in the upper row of Fig. S1. They are very similar to analytical solutions for an infinitely long, cylindrical waveguide, which are well known, for example, for optical fibers (shown in the lower row of Fig. S1. For the sake of clarity

in the following considerations of the LDOS, we continue with the analytical solutions of the cylindrical waveguide.

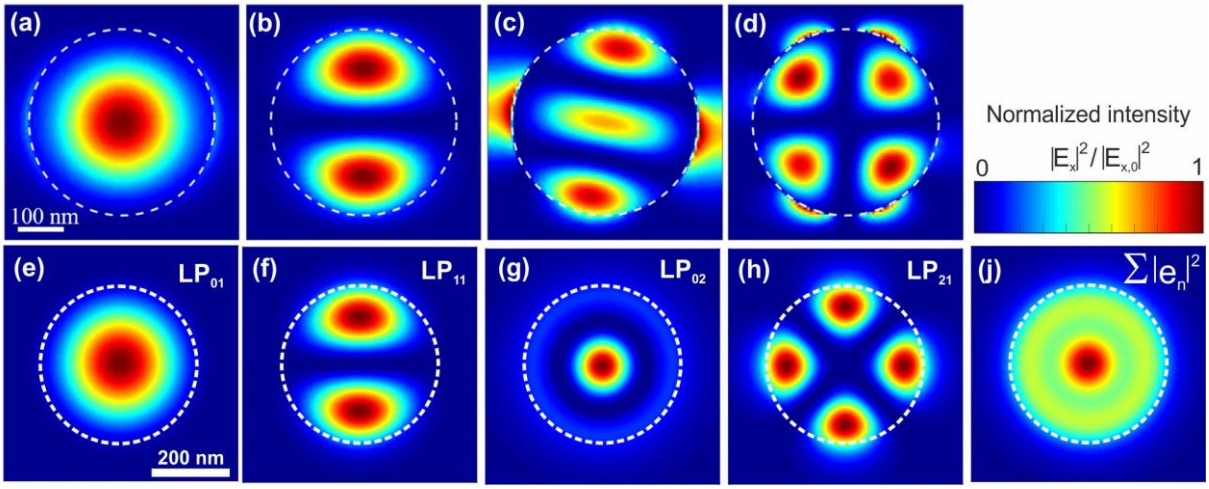

Fig. S1. (a)-(d) Solutions of the modes identified in FDTD simulations for a cylindrical structure of 200 nm diameter and 75 nm height, capped with a semi-ellipse to a total height of 150 nm and placed on top of a 100-nm thick film, both with refractive index of 3.04. The circumference is outlined by the broken white circles. The modes profiles are very similar to analytical calculations for a cylindrical waveguide, shown below. **(e)-(h)** Calculated mode intensity profiles for an infinitely long cylindrical waveguide with radius 200 nm and refractive index of 3.04, surrounded by air. Such a structure supports the **(e)** LP_{01}, **(f)** LP_{11}, **(g)** LP_{02}, and **(h)** LP_{21} guided modes. The LP_{11} and LP_{21} modes are degenerate: in addition to the profiles shown there exist profiles that are rotated such that the position of nodes and antinodes is switched. **(j)** The superposition of these four modes, including the degenerate solutions, represents the LDOS and is rotationally symmetric.

To calculate the eigenmodes of the Sb_2S_3 nanodot, we assume a cylindrical structure with radius $a = 200\,\text{nm}$, with the refractive index of Sb_2S_3 and surrounded by air. We find that over the wavelength range covered in our experiment, such a structure supports four guided modes. Using the standard nomenclature for fiber optical modes LP_{mp},[45,46] these are the LP_{01}, LP_{11}, LP_{02} and LP_{21} modes. Here, the first index, m, designates the angular momentum, i. e., the number of azimuthal nodes divided by 2, and the second index, p, gives the number of nodes in the radial coordinate r, including the node at $r \to \infty$. The cutoff wavelength for the highest order of these modes, the LP_{21} mode, is expected to lie close to the long-wavelength limit of the used laser spectrum. The intensity profiles of these four modes, calculated for a wavelength $\lambda = 800\,\text{nm}$ and $n_{Sb_2S_3}(\lambda = 800\,\text{nm}) = 3.04$, are plotted in Fig. S1(e)-(h). Note that the modes with angular momentum m=1 and m=2 are degenerate, such that the superposition and hence the LDOS is always rotationally symmetric (Fig. S1(j)). The waveguide modes are furthermore polarization degenerate and support electric field vectors in x- and y direction.

The sum over the eigenmodes in Eq. 6 is performed over the quantum numbers m and p of the bound fiber modes, as well as over the propagation constant $\beta_{m,p}(\omega)$, since, for every frequency ω in our spectral range and every bound mode (m, p) a wave exists that propagates along the fiber core with constant $\beta_{m,p}(\omega)$.

For the calculation of the projected LDOS shown in Fig. 4 in the main manuscript, we calculate the LDOS for a wavelength of 800 nm and assume a fixed tip dipole $\vec{p} = (0.3, 1, 0.2) = |\vec{p}| \cdot \hat{p}$ as excited by the laser focus. The orientation $\hat{u}$ required to calculate the projected LDOS then is the projection of $\hat{p}$ on the curved surface of the nanodot.

6 Influence of surface roughness

In order to demonstrate the influence of shape and surface structure of the nanodots on the sSNOM images, we selected a Sb_2S_3 nanodot with a relatively rough surface and recorded near-field maps using the APD and lock-in amplifier. In these measurements, we turn our attention to hotspots of high electric field intensity that are supported by nanoscopic features, like cracks and other surface defects.[54,55] The spatial extent of these hotspots may be less than the spatial resolution in SNOM, such that their apparent size can be resolution-limited. The recorded images of the selected nanodot are presented in Fig. S2.

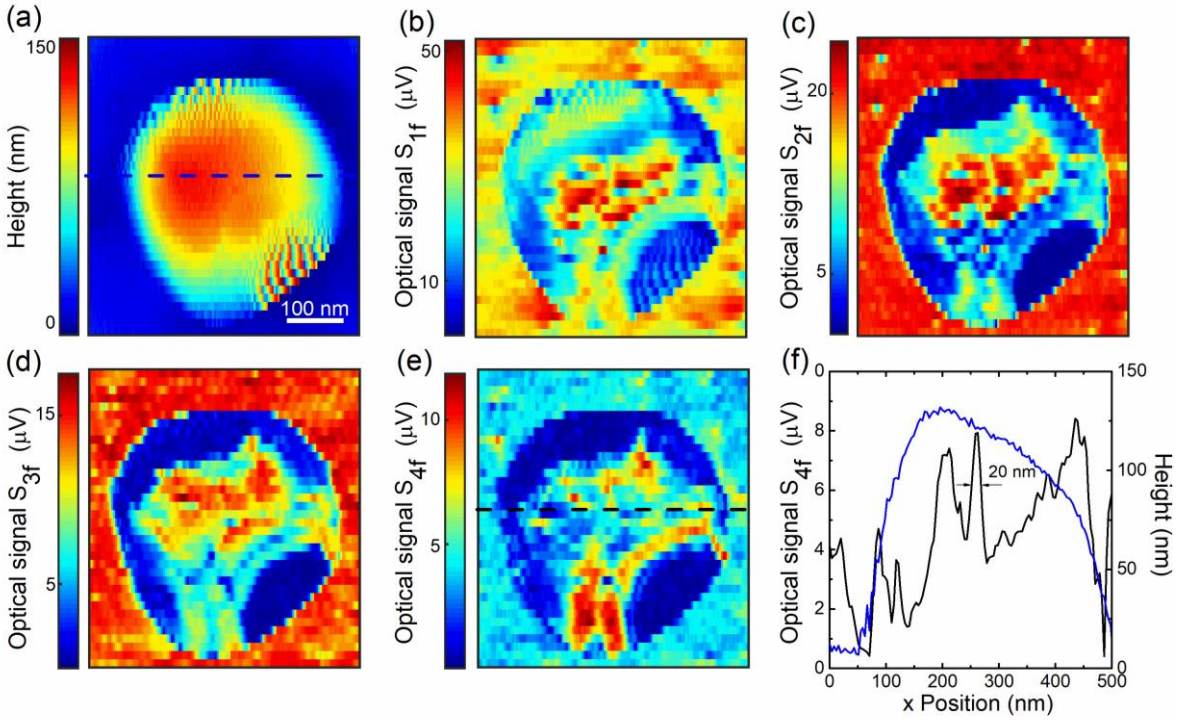

Figure S2. Near-field maps of an Sb2S3 nanodot. **(a)** The topographic image shows a slightly elliptic nanodot of approximately 320 nm by 380 nm, and of 150 nm height. With the height information provided by the atomic force microscope the surface seems smooth. **(b)-(e)** Maps of the optical signals recorded by demodulating at the first to fourth harmonic of the tip modulation frequency. **(f)** Cuts through the topographic map (blue curve) and the S_{4f} signal (black curve), along the dashed lines in Figs. (a) and (e), respectively. While the topology appears smooth, the S_{4f} signal is stronger structured and thereby reveals hotspots on the nanodot surface. The size of the features reaches down to 20 nm.

The topographic image (Fig. S2(a)) shows an almost circular nanodot of approximately 380 nm diameter and 150 nm height. With the height information provided by the atomic force microscope the surface seems smooth, except in the lower right area. Here, the height feedback became unstable. The optical signal demodulated with the fundamental tip modulation frequency, S_{1f} (Fig. S2(b)) reflects this height control oscillations. All optical signal maps show a strongly modulated signal in the central area of the nanodot, which may indicate localized electric fields due to surface roughness on a scale below the resolution limit of the AFM image. Figure S2(f) compares the topographical information (blue curve) and the S_{4f} signal (black curve) along a cross cut indicated by the dashed lines in Figs. S2(a) and (e), respectively. While the topology appears smooth, the S_{4f} signal is spatially structured, and indicates the mentioned hotspots on the nanodot surface. Evidently, for this nanodot, hotspot formation due to a finite amount of structural disorder dominates the SNOM images and thus the LDOS close to the surface. We deduce a spatial resolution of better than 20 nm from this measurement.